Regional Ionospheric Modeling with Raw Observations and Its Application in BDS Single-Frequency PPP

Kaitian Yuan and Wei Li(✉)

School of Geography and Information Engineering, China University of Geosciences, Wuhan, China
weili@cug.edu.cn

Abstract. The single-frequency precise point positioning (SFPPP) method has attracted widespread attention for its high precision and low cost, while the time delay caused by the ionosphere is one of the most problematic error sources in its data processing. With the completion of the BeiDou Global Navigation Satellite System (BDS), the users can access BDS positioning, navigation, and timing (PNT) service around the world. It is crucial to generate high-precision ionospheric products to improve the positioning accuracy and accelerate the convergence. However, the existing Global Ionospheric Map (GIM) products cannot satisfy the requirements of regional users for precise positioning, due to its poor spatial and temporal resolution. In this contribution, we estimate the biased slant ionospheric delay (SID) based on GPS dual-frequency (DF) raw observations from 30 stations in Australia and develop the regional ionospheric model (RIM). The performance of SFPPP with ionosphere corrected by RIM is evaluated using the BDS-2/BDS-3 observations from several stations and compared with the corresponding results obtained by CODE-GIM. Accounting for the long convergence time of uncombined (UC) SFPPP, we constrain the ionospheric delay parameter with RIM. And a time-varying weight constraint is attached to weaken the effect of RIM on the positioning accuracy after convergence. The results show that the RMS of the VTEC difference between RIM and CODE-GIM is better than 2 TECU. The RMS of BDS SFPPP with ionosphere corrected by RIM is better than 0.4 m and 0.3 m in north and east directions, respectively, and the average vertical accuracy is 0.53 m. The ionosphere-weighted (IW) SFPPP with RIM can significantly improve the convergence speed compared to the UC-SFPPP.

Keywords: Regional ionospheric modelling · Precise point positioning · BDS · Single-frequency · Ionosphere-weighted model

1 Introduction

Precise point positioning (PPP), proposed in 1997, is a single-receiver absolute positioning technique based on the use of external precision products and has gained more and more attention due to its global coverage and flexibility (Zumberge et al. 1997, Kouba

C. Yang and J. Xie (Eds.): *China Satellite Navigation Conference (CSNC 2022) Proceedings*, LNEE 910, pp. 198–208, 2022.
https://doi.org/10.1007/978-981-19-2576-4_17

and Héroux 2001, Li et al. 2018). With the progressive development of Global Navigation Satellite Systems (GNSS), the user demand for high-precision and low-cost positioning is growing. Therefore, how to reduce the hardware cost while ensuring accuracy has become a key issue for mass users. With the launch of the last BeiDou Global Navigation System (BDS-3) satellite on June 23, 2020, users can access BDS positioning, navigation, and timing (PNT) services around the world (Yang et al. 2020, Yang et al. 2021). Furthermore, The availability of multi-GNSS single-frequency (SF) receivers and their compatibility with BDS signals has contributed to the growth of interest in BDS SFPPP research (Su et al. 2021, Zhu et al. 2021).

The ionospheric delay can reach several or even hundreds of meters, which will severely degrade the positioning performance (Li et al. 2019). Since SFPPP cannot eliminate the first-order effects of the ionosphere with an ionosphere-free (IF) combination, the time delay caused by the ionosphere becomes one of the most serious error sources in its data processing. However, the existing Global Ionospheric Map (GIM) products only have an accuracy of 2–8 TECU (Total Electron Content Unit), which is equivalent to a pseudorange error of 0.3–1.3 m at the BDS B1 frequency (Liu et al. 2019). Consequently, it is crucial to generate high-precision ionospheric products to improve the positioning accuracy and accelerate the convergence.

GNSS-based vertical total electron content (VTEC) modeling approach has received extensive applications with the advantages of high accuracy, all-weather availability, and global coverage (Mannucci et al. 1998, Li et al. 2015). It is necessary to note that current ionospheric products are generated by the Carrier-to-Code Leveling (CCL) method, which is easily affected by code noises, multipath effects, and arc length (Zhang 2016, Li et al. 2021). The undifferenced and uncombined PPP based on raw observations can effectively address this deficiency and provide a better alternative for the extraction of slant ionospheric delays (SID) (Liu et al. 2018).

On the other hand, another effective solution for SFPPP is to estimate the SID parameters, and the full rank uncombined (UC) SFPPP functional model is deduced by Re-parameterization and S-bias theory (Teunissen 1985, Zhao et al. 2021). Accounting for the long convergence time of UC-SFPPP, the external ionospheric information is used as pseudo-observations to constrain the SIDs. And a time-varying weight constraint is attached to weaken the effect of ionospheric products on the positioning accuracy after convergence (Cai et al. 2017).

This study focuses on the development of a highly accurate regional ionospheric model (RIM) and its further use in SFPPP to improve positioning performance and accelerate convergence. Firstly, the regional VTEC modeling method and two algorithmic models of SFPPP are presented in detail. Then, the regional ionospheric model (RIM) over Australia is developed with the raw observations. The positioning performance and convergence time of BDS SFPPP with the RIM are also evaluated. Finally, the research findings and concluding remarks are summarized in Sect. 4.

2 Function Model

2.1 PPP with Raw Observations

The satellite signal is affected by the ionosphere as it passes through the atmosphere, and we can extract this SID from the UC-PPP. The raw carrier phase Φ_r^s and pseudorange P_r^s observations can be expressed as follows (Zhang et al. 2012):

$$\begin{cases} P_r^s(i) = \rho_r^s + (c \cdot dt_r - c \cdot dt^s) + T_r + \gamma_i I_{r,1}^s + HD_{r,i} - HD_i^s + \varepsilon_{P_i} \\ \Phi_r^s(i) = \rho_r^s + (c \cdot dt_r - c \cdot dt^s) + T_r - \gamma_i I_{r,1}^s + \lambda_i N_{r,i}^s + \varepsilon_{\Phi_i} \end{cases} \tag{2.1}$$

where indices i, s, and r refer to the frequency band, satellite, and receiver, respectively; dt_r and dt^s are the clock biases at receiver and satellite, while T_r denotes the zenith tropospheric delay; $I_{r,1}^s$ is the SID on L1 signal and the frequency-dependent factor γ_i can be expressed as $\gamma_i = (f_i/f_1)^2$; $HD_{r,i}$ and HD_i^s are the frequency-related receiver and satellite code hardware delays; $N_{r,i}^s$ denotes the phase ambiguity; ε_{P_i} and ε_{Φ_i} are the effects of code and phase unmodeled errors, including multipath effects and observation noise.

Considering the IF combinations of satellite code hardware delays in the IGS precision satellite clock products, the observation equations can be given after parameter reformulation (Zhou et al. 2018):

$$\begin{cases} P_r^s(i) = \rho_r^s + \left(c \cdot d\tilde{t}_r - c \cdot d\tilde{t}^s\right) + T_r + \gamma_i \tilde{I}_{r,1}^s + \varepsilon_{P_i} \\ \Phi_r^s(i) = \rho_r^s + \left(c \cdot d\tilde{t}_r - c \cdot d\tilde{t}^s\right) + T_r - \gamma_i \tilde{I}_{r,1}^s + \lambda_i \tilde{N}_{r,i}^s + \varepsilon_{\Phi_i} \end{cases} \tag{2.2}$$

where symbols with identifiers indicate the reparameterized estimable parameters; $\tilde{I}_{r,1}^s$ contains the satellite and receiver differential code bias (DCB) and is written as:

$$\tilde{I}_{r,1}^s = I_{r,1}^s - \frac{c}{\gamma_2 - 1}\left(DCB_r + DCB^s\right) \tag{2.3}$$

where $DCB_r = HD_{r,1} - HD_{r,2}$ and $DCB^s = HD_1^s - HD_2^s$.

2.2 Regional Ionospheric VTEC Modeling

As Eq. (2.3) shows, the estimated SID from the UC-PPP is biased by the receiver and satellite DCBs (RDCB, SDCB) and can be transformed to slant total electron contents (STEC) (Wang et al. 2020):

$$\widetilde{STEC} = \tilde{I}_{r,1}^s \cdot \frac{f_1^2}{40.28} \tag{2.4}$$

where f_1 stands for the frequency of the carrier. To model the ionosphere over a region, the STECs are mapped into VTECs using the single-layer mapping function, which can be written as (Li et al. 2020):

$$\begin{cases} VTEC = Mf \cdot STEC \\ Mf = \cos\left(\arcsin\left(\frac{R}{R+H}\sin(Z)\right)\right) \end{cases} \tag{2.5}$$

where Z is the zenith angle at the receiver; R is the earth's radius ($R = 6378137$ m), while H refers to the height of the assumed single-layer ionosphere ($H = 450$ km).

In this contribution, an ionospheric spherical harmonic function is used to characterize the spatiotemporal variation of regional ionospheric VTEC, which can be presented as follows (Liu et al. 2018):

$$VTEC = \sum_{n=0}^{n_{\max}} \sum_{m=0}^{n} \overline{P}_{nm}(\sin\varphi')\left(a_{nm}\cos(m\lambda') + b_{nm}\sin(m\lambda')\right) \tag{2.6}$$

where φ' and λ' are the geomagnetic latitude and longitude of the intersecting pierce point (IPP) in the sun-fixed reference frame, respectively; $\overline{P}_{nm}$ denotes the normalized associated Legendre function, while a_{nm} and b_{nm} are the normalized coefficients.

To obtain more stable results and reduce parameters in regional ionospheric modeling, the estimated SDCBs are fixed to the CODE monthly-mean values in this study, and the remaining RDCBs are estimated as constants. Based on the above theories, the RDCBs and ionospheric coefficients can be derived by the least-squares method.

2.3 Function Model of SFPPP

According to Eq. (2.1) and (2.2), the observations of the first frequency of BDS is adopted and the biased SIDs contains the SDCBs after the introduction of the precision products. To avoid the rank deficit, the SDCBs are fixed to the CAS day-mean values. Then, the algorithms of ionosphere-corrected (IC) SFPPP can be given after parameter reformulation (Zhao et al. 2021):

$$\begin{cases} P_r^s(1) = \rho_r^s + c \cdot d\tilde{t}_r + T_r + \varepsilon_{P_1} \\ \Phi_r^s(1) = \rho_r^s + c \cdot d\tilde{t}_r + T_r + \tilde{N}_{r,1}^s + \varepsilon_{\Phi_1} \end{cases} \tag{2.7}$$

Different from IC-SFPPP, the external ionospheric information is used as pseudo-measurement in ionosphere-weighted (IW) SFPPP (Zhu et al. 2021).

$$\begin{cases} P_r^s(1) = \rho_r^s + c \cdot d\tilde{t}_r + T_r + I_{r,1}^s + \frac{f_2^2}{f_1^2 - f_2^2} DCB^s + \varepsilon_{P_1} \\ \Phi_r^s(1) = \rho_r^s + c \cdot d\tilde{t}_r + T_r - I_{r,1}^s + \tilde{N}_{r,1}^s + \varepsilon_{\Phi_1} \\ \tilde{I}_{r,1}^s = I_{r,1}^s + \varepsilon_{ion} \end{cases} \tag{2.8}$$

where, $\tilde{I}_{r,1}^s$ denotes the SIDs obtained by external ionospheric products, while ε_{ion} is the noise of pseudo- observations.

The SDCBs are separated from the SIDs with the accession of ionospheric pseudo-observations and are fixed to the CAS day-mean values. Given the accuracy limitations of external ionospheric products, the virtual ionospheric observations are given more significant weight at the beginning of the SFPPP process to speed up convergence, and their weight is gradually reduced to obtain better positioning performance. This time-varying weighting scheme can be expressed as (Cai et al. 2017):

$$\sigma^2 = \sigma_0^2 + \alpha \cdot \Delta t \tag{2.9}$$

where σ^2 is the initial variance of the pseudo-observations; α is variance change rate over time, while Δt refers the filtering time.

3 Datasets and Experiments

3.1 Data Collection and Processing Strategy

In this study, we collected GPS dual-frequency (DF) observations of 30 stations in Geoscience Australia (GA) from DOY 214 to 220 in 2021 for the regional ionospheric VTEC modeling, and the distribution of stations is shown in Fig. 1. In addition, the BDS B1 observations from another 10 stations, indicated by blue symbols, are selected to verify the positioning performance of SFPPP with RIM.

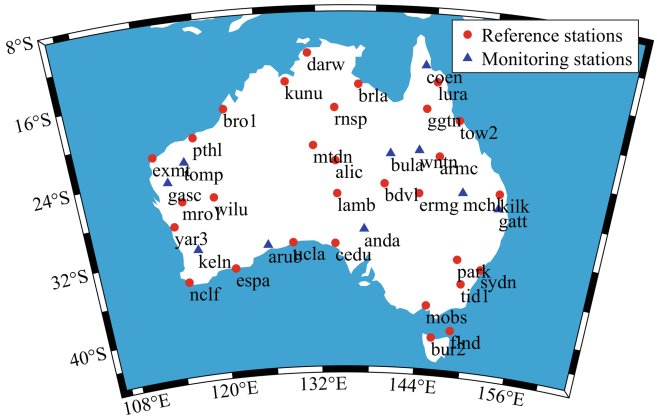

Fig. 1. Distribution of the selected reference stations and monitoring stations in Australia

Three SFPPP models are applied for this experiment, namely IC-SFPPP, IW-SFPPP and UC-SFPPP. Except for the ionospheric delay, all other parameters of the three SFPPP models are estimated in the same way. Table 1 summarizes our parameter settings of the three SFPPP modes:

Table 1. Data processing strategies for SFPPP

Item	SFPPP
Position	Kinematic
Signal selection	BDS2/BDS3: B1
Clock & orbits	GFZ products
Troposphere modeling	Saastamoinen model + random walk process
Elevation cutoff	10°
Sampling interval	30 s
Ionosphere delay	IC-SFPPP: Corrected IW-SFPPP: Slant Delay + Constraint UC-SFPPP: Estimated
Satellite DCB	CAS

For selected stations, the average coordinates of the GPS static DF-PPP results are used as the reference position. And the convergence time is defined as the first epoch in which the positioning errors in the horizontal and vertical directions are less than 0.3 m, 0.6 m for 10 min.

3.2 Validation of Regional VTEC Modeling

The gridded ionospheric VTEC map can be generated hourly based on the estimated model coefficients. The performance of the RIM over Australia was verified by the comparison with the CODE-GIM. Figure 2 shows the VTEC differences between RIM and CODE-GIM every four hours in DOY 214, 2020, with a spatial resolution of $1° \times 1°$.

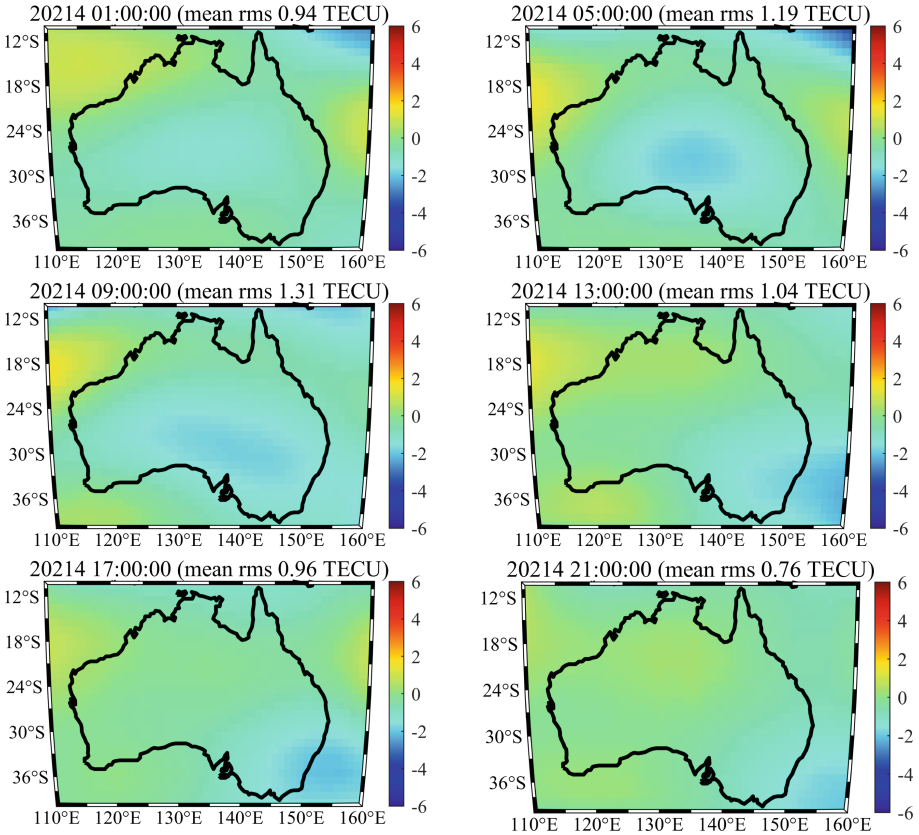

Fig. 2. RMS of VTEC differences between UC-PPP method and CODE-GIM

As shown in Fig. 2, as CODE has also selected several stations in Australia for the GIM generation, there is good consistency between RIM and CODE-GIM. The RMSs of the VTEC differences are better than 2 TECU over all seven days of the experiment.

Additionally, the differential STECs (dSTEC) retrieved from the RIM are also evaluated according to the approach proposed by Feltens et al. (Feltens et al. 2011) and the results are exhibited in Fig. 3. The dSTEC is defined as the difference between the STEC at any point along a continuous arc and the STEC extracted when the satellite is at its highest elevation (Feltens et al. 2011). It can be seen that the average RMS value of RIM (1.73 TECU) is the smallest among the three methods after removing some outliers, which shows the superiority of this modeling method. It should be noted that the CCL method has the largest deviation (2.07 TECU), which is related to its susceptibility to pseudorange noise and multipath effects.

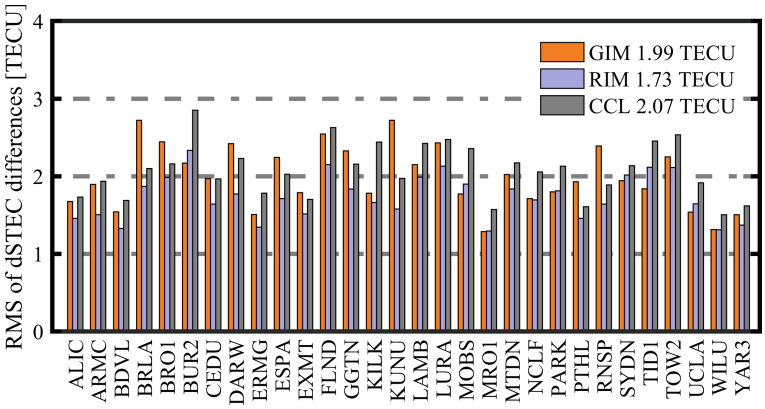

Fig. 3. RMS of dSTEC differences for GIM, RIM, and CCL

3.3 Validation of IC-SFPPP with RIM

Figure 4 illustrates the positioning error series of BDS kinematic SFPPP with ionosphere corrected by RIM and GIM, respectively. The UC-SFPPP results in the north, east, and up directions are also presented for comparison. It can be seen that the IC-SFPPP with GIM has more discrete points, while the corresponding results for RIM are smoother. In general, the horizontal accuracy of IC-SFPPP is significantly better than the vertical, while the east component is usually the most accurate of all three directions. For further comparison, Table 2 provides the RMS statistics for the three coordinate components of each station.

From the data in Table 2, it is apparent that using RIM to correct the ionosphere rather than GIM performs well in the BDS SFPPP, especially in the vertical direction. At some specific stations, the RMS of IC-SFPPP with RIM is even at the same level of performance as the UC-SFPPP. Overall, The average accuracies of IC-SFPPP with RIM in the three directions reach 32.64 cm, 16.7 cm, and 53.13 cm, respectively, improving by 24.9%, 27.2%, and 33.6% compared with the corresponding results using the GIM.

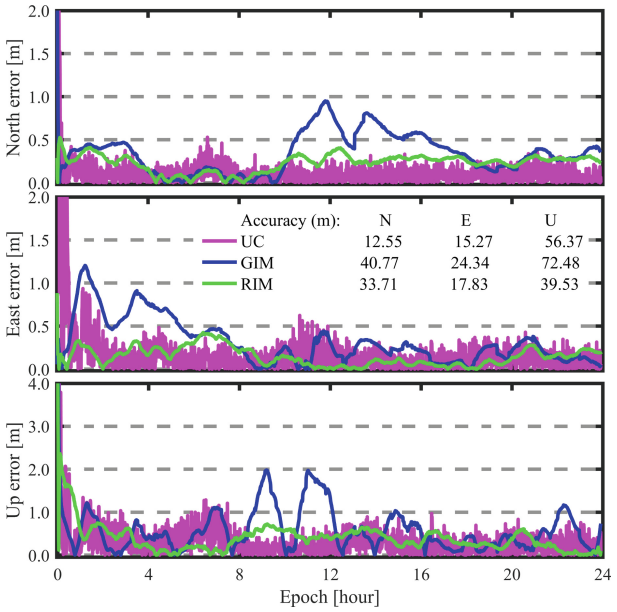

Fig. 4. SFPPP errors for different processing strategies with BDS-2/BDS-3 observations at station TOMP on DOY 214, 2020

Table 2. RMS statistics of BDS IC-SFPPP coordinate deviations (cm)

Station	RIM			GIM		
	N	E	U	N	E	U
ANDA	35.52	15.80	61.14	45.95	22.96	84.24
ARUB	31.80	9.27	61.02	37.24	14.23	64.30
BULA	30.15	13.81	51.56	48.63	20.88	55.87
COEN	30.68	26.70	63.26	45.60	40.45	83.58
GASC	32.82	21.39	58.59	49.56	27.44	97.31
GATT	33.79	21.36	45.04	66.28	31.92	104.25
KELN	39.34	15.46	48.89	37.49	13.32	57.41
MCHL	26.44	18.93	50.38	61.03	28.62	89.13
TOMP	32.40	15.55	49.07	56.73	22.22	99.69
WNTN	33.51	21.77	42.38	41.87	25.28	64.60

3.4 Assessment of Convergence Performance in IW-SFPPP

In this part, the collected BDS B1 observations are used to assess the convergence time of IW-SFPPP with RIM. Figure 5 indicates the positioning error statistics for the IW-SFPPP at the station WNTN and provides the corresponding results of UC-SFPPP for comparison. In addition, Fig. 6 presents the average convergence times for UC-SFPPP and IW-SFPPP for all stations during the experimental period.

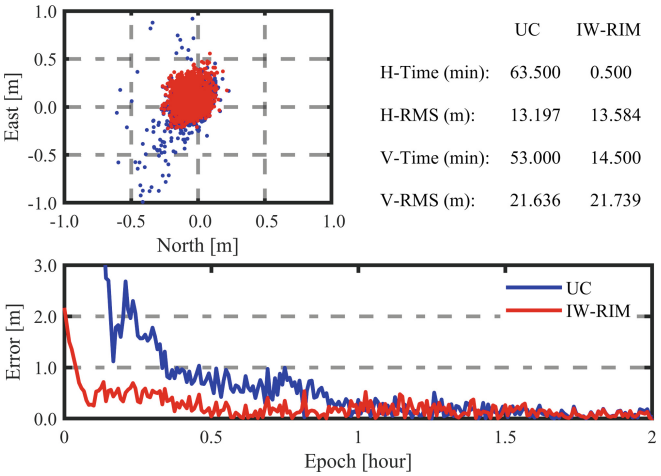

Fig. 5. Accuracy and convergence performance of BDS SFPPP kinematic positioning at station WNTN on DOY 214, 2020

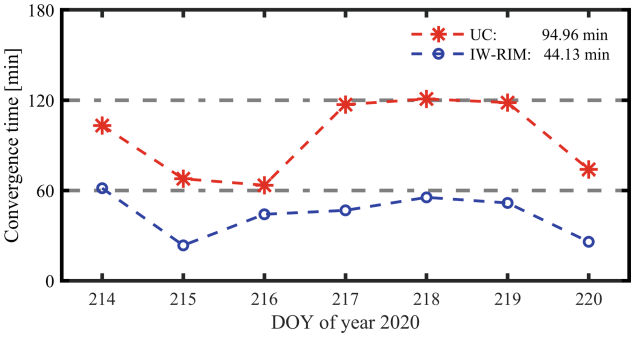

Fig. 6. Convergence time statistics for BDS UC-SFPPP and IW-SFPPP

As can be seen in Figs. 5 and 6, the introduction of the RIM constraint on ionospheric delay can significantly improve the convergence time of UC-SFPPP. Undoubtedly, the RIM plays a crucial role in the early filter processing in the IW-SFPPP with time-varying weights, while its impact on the positioning accuracy is negligible after convergence. Overall, the additional ionospheric constraint improves the convergence time from 94.96 min to 44.13 min, improving by 53.5%.

4 Conclusion

Since SFPPP is unable to eliminate first-order ionospheric effects using an ionosphere-free combination, the time delay caused by the ionosphere is one of the most problematic sources of error in its processing. Therefore, generating a highly accurate regional ionospheric model is important to improve the SFPPP positioning performance and convergence time.

In this article, we modeled regional VTEC over Australia based on GPS raw observations and compared it to the CODE-GIM with an overall accuracy better than 2 TECU. Additionally, the dSTECs retrieved from the RIM are also assessed by comparison with the CODE-GIM. The RMS values of the dSTECs extracted by RIM, CODE-GIM and CCL methods are 1.73, 1.99 and 2.07 TECU, respectively.

Then, the generated RIM is applied to two BDS SFPPP models. Firstly, the positioning performance of SFPPP with ionosphere corrected by RIM rather than GIM is significantly improved, by 24.9%, 27.2%, and 32.4% in the N, E, and U directions respectively. As for IW-SFPPP, filter convergence can be considerably accelerated with the inclusion of the RIM. Furthermore, the impact on positioning accuracy after convergence is negligible with the time-varying weights. As a result, RIM offers a new option for regional users for high accuracy, low-cost positioning with BDS observations.

Acknowledgments. This research was supported by the National Science Foundation of China (grant No. 41804033 and No. 42174043).

References

Cai, C., Gong, Y., Gao, Y., Kuang, C.: An approach to speed up single-frequency PPP convergence with quad-constellation GNSS and GIM. Sensors **17**, 1302 (2017)

Feltens, J., et al.: Comparative testing of four ionospheric models driven with GPS measurements. Radio Sci. **46**, 1–11 (2011)

Kouba, J., Héroux, P.: Precise point positioning using IGS orbit and clock products. GPS Solutions **5**, 12–28 (2001)

Li, W., Wang, G., Mi, J., Zhang, S.: Calibration errors in determining slant Total Electron Content (TEC) from multi-GNSS data. Adv. Space Res. **63**, 1670–1680 (2019)

Li, X., Li, X., Yuan, Y., Zhang, K., Zhang, X., Wickert, J.: Multi-GNSS phase delay estimation and PPP ambiguity resolution: GPS, BDS, GLONASS, Galileo. J. Geodesy **92**(6), 579–608 (2017). https://doi.org/10.1007/s00190-017-1081-3

Li, Z., et al.: IGS real-time service for global ionospheric total electron content modeling. J. Geodesy **94**, 32 (2020)

Li, Z., et al.: Status of CAS global ionospheric maps after the maximum of solar cycle 24. Satell. Navig. **2**, 19 (2021)

Li, Z., Yuan, Y., Wang, N., Hernandez-Pajares, M., Huo, X.: SHPTS: towards a new method for generating precise global ionospheric TEC map based on spherical harmonic and generalized trigonometric series functions. J. Geod. **89**, 331–345 (2015)

Liu, T., Zhang, B., Yuan, Y., Li, M.: Real-Time Precise Point Positioning (RTPPP) with raw observations and its application in real-time regional ionospheric VTEC modeling. J. Geodesy **92**(11), 1267–1283 (2018). https://doi.org/10.1007/s00190-018-1118-2

Liu, T., Zhang, B., Yuan, Y., Zhang, X.: On the application of the raw-observation-based PPP to global ionosphere VTEC modeling: an advantage demonstration in the multi-frequency and multi-GNSS context. J. Geodesy **94**(1), 1–20 (2019). https://doi.org/10.1007/s00190-019-01332-z

Mannucci, A.J., Wilson, B.D., Yuan, D.N., Ho, C.H., Lindqwister, U.J., Runge, T.F.: A global mapping technique for GPS-derived ionospheric total electron content measurements. Radio Sci. **33**, 565–582 (1998)

Su, K., Jin, S., Jiang, J., Hoque, M., Yuan, L.: Ionospheric VTEC and satellite DCB estimated from single-frequency BDS observations with multi-layer mapping function. GPS Solutions **25**(2), 1–17 (2021). https://doi.org/10.1007/s10291-021-01102-5

Teunissen, P.: Zero order design: generalized inverses, adjustment, the datum problem and S-transformations. In: Grafarend, E.W., Sansò, F. (eds.) Optimization and Design of Geodetic Networks, pp. 11–55. Springer, Heidelberg (1985). https://doi.org/10.1007/978-3-642-70659-2_3

Wang, H., Sui, Y., Wang, D., Fu, H., Feng, S.: Un-difference PPP method and performance assessment based on regional ionospheric model. In: Sun, J., Yang, C., Xie, J. (eds.) CSNC 2020. LNEE, vol. 651, pp. 684–695. Springer, Singapore (2020). https://doi.org/10.1007/978-981-15-3711-0_61

Yang, Y., et al.: Featured services and performance of BDS-3. Science Bulletin (2021)

Yang, Y., Mao, Y., Sun, B.: Basic performance and future developments of BeiDou global navigation satellite system. Satell. Navig. **1**(1), 1–8 (2020). https://doi.org/10.1186/s43020-019-0006-0

Zhang, B.: Three methods to retrieve slant total electron content measurements from ground-based GPS receivers and performance assessment. Radio Sci. **51**, 972–988 (2016)

Zhang, B., Ou, J., Yuan, Y., Li, Z.: Extraction of line-of-sight ionospheric observables from GPS data using precise point positioning. Sci. China Earth Sci. **55**, 1919–1928 (2012)

Zhao, C., Zhang, B., Zhang, X.: SUPREME: an open-source single-frequency uncombined precise point positioning software. GPS Solutions **25**(3), 1–8 (2021). https://doi.org/10.1007/s10291-021-01131-0

Zhou, F., Dong, D., Li, W., Jiang, X., Wickert, J., Schuh, H.: GAMP: An open-source software of multi-GNSS precise point positioning using undifferenced and uncombined observations. GPS Solutions **22**(2), 1 (2018). https://doi.org/10.1007/s10291-018-0699-9

Zhu, S., Yue, D., He, L., Chen, J., Liu, Z.: Comparative analysis of four different single-frequency PPP models on positioning performance and atmosphere delay retrieval. Adv. Space Res. **67**, 3994–4010 (2021)

Zumberge, J.F., Heflin, M.B., Jefferson, D.C., Watkins, M.M., Webb, F.H.: Precise point positioning for the efficient and robust analysis of GPS data from large networks. J. Geophys. Res. Solid Earth **102**, 5005–5017 (1997)